The final publication is available at Springer via http://dx.doi.org/10.1007/s11071-009-9496-x

Computational model for calculating the dynamical behaviour of generators caused by unbalanced magnetic pull and experimental validation

Paolo Pennacchi
Dipartimento di Meccanica
Politecnico di Milano
I-20156, Milan, Italy
paolo.pennacchi@polimi.it

Abstract

The modelling of the unbalanced magnetic pull (UMP) in generators and the experimental validation of the proposed method are presented in this paper.

The UMP is one of most remarkable effects of electromechanical interactions in rotating machinery. As a consequence of the rotor eccentricity, the imbalance of the electromagnetic forces acting between rotor and stator generates a net radial force. This phenomenon can be avoided by means of a careful assembly and manufacture in small and stiff machines, like electrical motors. On the contrary, the eccentricity of the active part of the rotor with respect to the stator is unavoidable in big generators of power plants, because they operate above their first critical speed and are supported by oil-film bearings.

In the first part of the paper, a method aimed to calculate the UMP force is described. This model is more general than those available in literature, which are limited to circular orbits. The model is based on the actual position of the rotor inside the stator, therefore on the actual air-gap distribution, regardless of the orbit type. The closed form of the non-linear UMP force components is presented.

In the second part, the experimental validation of the proposed model is presented. The dynamical behaviour in the time domain of a steam turbo-generator of a power plant is considered and it is shown that the model is able to reproduce the dynamical effects due to the excitation of the magnetic field in the generator.

Key words

Unbalanced magnetic pull, Electromechanical interactions, Generators, Non-linear effects, Rotor dynamics.

1. Introduction

The phenomenon of the unbalanced magnetic pull (UMP) is rather common in electrical rotating machinery. In general terms, if the air-gap distribution between the rotor and the stator is uniform in a cross section, the electromagnetic forces are balanced. When the rotor is eccentric with respect to the stator, the air-gap distribution is not uniform and causes the imbalance of the electromagnetic forces. Consequently a net radial force is generated, which pulls the rotor towards the stator in the direction of the minimum air-gap.

The studies present in literature about the UMP can be roughly classified in three groups: small electrical motors, large electrical motors and generators.

As it concerns small electrical motors, the UMP forces can be considerable because the air-gaps are very small (0.3-3 mm). However rotor-dynamic problems are often negligible in these machines, since their rotors are quite stiff, and the studies are focused on electrical aspects. The first models presented, to calculate the UMP, were related to small motors (Bradford [1], Binns and Dye [2] and Dorrel et al. [3] [4] [5]). In some cases, these models are also supported by experimental validation, like the tests performed by Dorrel et al. [6] [7] [8].

In the case of large electrical motors, the air-gap is not so small as before, but UMP nevertheless has significant effects on the mechanical dynamic response of the machine. Interesting analyses are presented by Belmans et al. [9] and more recently by Holopainen, Arkkio et al. [10] [11] [12] [13] [14].

As regards generators, the effects of relative misalignment between the rotor and the stator have been described [15] since the 60's, but the analysis and the modelling of the phenomenon is more recent. Actually, a further distinction has to be made between slim and squat generators.

Slim generators, with one or two pole-pairs, have a large air-gap (30-100 mm) and the rotor is rather flexible, therefore rotor-dynamic problems are not negligible. Stoll [16] proposes a theoretical model to calculate the UMP forces that is based on static eccentricity, and presents a simulated case using data of a real machine. Guo et al. [17] adapt the model developed for electrical motors by Dorrel [5] to generators and consider dynamic eccentricity too. An approximate expression for the air-gap allows these authors to express the UMP in analytic closed form for different pole-pairs and the simulation of the dynamical behaviour of a simple Jeffcott-rotor-like machine is presented under the effect of the UMP.

Squat generators have a small air-gap (10-15 mm), but the rotor is very stiff. Theoretical models for UMP calculation were presented by Nabil and Toliyat [18] [19], while the effects on the stability of a hydraulic generator are studied by means of a simple model by Gustavsson and Aidanpää [20].

A common characteristic of the previous studies proposed in literature about generators is the use of very simplified modelling for the rotor-dynamic part, which hardly can simulate the dynamical behaviour of actual machines, especially for slim machines. Some of them use an accurate 3D modelling for the electromagnetic forces but then apply a modal model for the rotor (or a Jeffcott rotor) in order to reduce the number of the degrees of freedom (d.o.f.s) in the dynamic analysis of the rotor.

The approach proposed here is different, since the validation requires comparing the measured dynamical behaviour of a real machine with the simulated one, and the rotor model is made with finite beam elements. On the contrary, for the electromechanical interaction, the approach of the air-gap permeance is used and it allows a closed form for the UMP forces to be obtained. This does not require increasing the order of the dynamical model and allows simulations in the time domain to be performed in an acceptable computational time. Obviously the implementation of a 3D modelling for the electromechanical interaction, along with a finite element model for the rotor would be more accurate, but would also require unacceptable computational times to be integrated in the time domain, due to the huge number of d.o.f.s.

Moreover, no experimental validation of the proposed models for generators has been presented to the author's knowledge. The present paper overrides these limitations and introduces a way to calculate the UMP starting from a general orbit of a flexible rotor inside the stator.

The first part of the paper summarizes the calculation method, described in detail in [21], introducing the expression for the air-gap distribution, depending on the instantaneous position of the rotor inside the stator. The UMP calculated by means of the air-gap permeance approach is consequently a function of both time and relative position of the rotor and stator.

In the second part of the paper, the validation of the calculation method is presented. Since it is rather difficult, although not impossible, to directly measure the UMP forces in a real machine, their effect can be evaluated indirectly by means of the vibrational behaviour of the machine. Therefore, the dynamical behaviour of a slim generator of a power plant is analyzed and the effects due to the UMP are reproduced by means of model based simulation of the machine response. The experimental data are related to a no-load condition, once the operating speed is reached, after and before the excitation of the air-gap magnetic flux. In this condition, thermal bows caused by Joule effect that could influence the machine behaviour should not be present.

2. Modelling of the UMP under general air-gap distribution

Traditional models of UMP distinguish between static eccentricity and dynamic eccentricity. In the first case, the position of minimum radial air-gap is fixed in space: the rotor is symmetrical with

respect to its axis and rotates about it. In the second case, the position of minimum radial air-gap rotates with the rotor: in the case of a machine, which can be considered as rigid, the shaft axis does not coincide with the rotor axis (the rotor does not rotate about its axis).

The difference between static and dynamic eccentricity is actually relevant in the case of electric motors of small to medium size in which very stiff bearings, normally rolling bearings, are used and the motor operates below its first critical speed.

High-speed turbo-generators operate above their first critical speed, therefore they are flexible and the position of minimum radial length of the air-gap rotates with the rotor. Actual rotor direct orbits are not circular as assumed in [17] and [16]. Since oil-film bearing are used, the oil-film forces determine the rotor centreline to describe a path during the run-up, therefore the rotor centreline is not generally concentric with the stator (figure 1). Moreover, the dynamical deformation of the rotor produces an air-gap distribution that is not constant along the span of the rotor, while the dynamical deformation depends on the exciting systems applied to the machine. For this reason, the air-gap distribution has to be defined for each section of the machine slotted part.

Figure 2 shows the relative position of the rotor and the stator in a general time instant t, for a generator section, and the average air-gap length is intentionally magnified for graphical clearness. The reference system $S'(x', \mathrm{O}', y')$ is fixed and centred in the stator centre O', while the reference system $S''(x'', \mathrm{O}'', y'')$ has its centre O'' that corresponds to the rotor centreline. Due to the presence of lateral vibrations, the rotor centre O describes an orbit around the centreline. Therefore, the eccentricity between the stator and the rotor centre is determined by two components: the offset $\overrightarrow{\mathrm{O}'\mathrm{O}''}$ due to the centreline path during the run-up and the lateral vibration $\overrightarrow{\mathrm{O}''\mathrm{O}}$ of the rotor. The position of the rotor centre $\mathrm{P}_0 \equiv \mathrm{O}$ in a general time instant t depends on the previous time history and on the exciting systems acting on the shaft. The reference system $S(x, \mathrm{O}, y)$ is centred in the rotor centre. Since the aim is to determine the air-gap length radial distribution, the angular relative position of S and S' is not relevant and for simplicity the reference axes are considered as parallel.

The equation of the stator circumference $\Gamma_2^{(S)}$ in the reference S is:

$$\left(x - x_{\mathrm{O}'}\right)^2 + \left(y - y_{\mathrm{O}'}\right)^2 = r_s^2 \tag{1}$$

in which $\mathbf{x}_{\mathrm{O}'} = x_{\mathrm{O}'}(t)\,\mathbf{i} + y_{\mathrm{O}'}(t)\,\mathbf{j}$ indicates the position vector of O' in the reference system S in a general time instant t. These values are actually the absolute vibration of rotor with respect to the stator centre. The equation of a general line $\Gamma_3^{(S)}$ in the reference system S passing through P_0 is:

$$\Gamma_3^{(S)}: \quad y = x \tan\beta, \ |\beta| \neq \pi/2 \tag{2}$$

The angle β is called *spatial angle*. If $|\beta| \neq \pi/2$ the intersections $\{P_1, P_2\} = \Gamma_3 \cap \Gamma_2$ between the general line passing through P_0 and the stator are obtained by replacing eq. (2) in eq. (1):

$$\{P_1, P_2\}^{(S)} : \begin{cases} (x - x_{O'})^2 + (x \tan\beta - y_{O'})^2 = r_s^2 \\ y = x \tan\beta \end{cases}, |\beta| \neq \pi/2 \tag{3}$$

After some algebraic manipulations, first equation of eq. (3) becomes:

$$x^2 - 2x\left(x_{O'} \cos^2\beta + y_{O'} \cos\beta \sin\beta\right) - r_s^2 \cos^2\beta + x_{O'}^2 \cos^2\beta + y_{O'}^2 \cos^2\beta = 0 \tag{4}$$

Eq. (4) is a 2nd order algebraic equation in the unknown x and has two solutions: for $|\beta| < \pi/2$ the solution with the sign + corresponds to point P_1 in figure 2 and the solution with sign – to point P_2. For $-\pi < \beta < -\pi/2 \cup \pi/2 < \beta \leq \pi$ the solution with the sign + corresponds to point P_2, that with sign – to point P_1. After some simplifications, co-ordinates of points P_1 and P_2 result:

$$\{P_1, P_2\}^{(S)} :$$
$$\begin{cases} x_{P_1,P_2} = x_{O'} \cos^2\beta + y_{O'} \cos\beta \sin\beta \pm \sqrt{\cos^2\beta \left(r_s^2 - \left(y_{O'} \cos\beta - x_{O'} \sin\beta\right)^2\right)} \\ y_{P_1,P_2} = x_{O'} \cos\beta \sin\beta + y_{O'} \sin^2\beta \pm \tan\beta \sqrt{\cos^2\beta \left(r_s^2 - \left(y_{O'} \cos\beta - x_{O'} \sin\beta\right)^2\right)} \end{cases}, |\beta| \neq \frac{\pi}{2} \tag{5}$$

The special case $|\beta| = \pi/2$ is not important as explained later. The equation of the rotor circumference $\Gamma_1^{(S)}$ is:

$$x^2 + y^2 = r_r^2 \tag{6}$$

If $|\beta| \neq \pi/2$, the intersections $\{P_3, P_4\} = \Gamma_3 \cap \Gamma_1$ between the general line passing through P_0 and the rotor are given replacing eq. (2) in eq. (6):

$$\{P_3, P_4\}^{(S)} : \begin{cases} x^2 + y^2 = r_r^2 \\ y = x \tan\beta \end{cases} \rightarrow \begin{cases} x^2 + x^2 \tan^2\beta = r_r^2 \\ y = x \tan\beta \end{cases}, |\beta| \neq \frac{\pi}{2} \tag{7}$$

After some manipulation, first equation of eq. (7) becomes:

$$x^2 - r_r^2 \cos^2\beta = 0 \tag{8}$$

Eq. (8) has two solutions: for $|\beta| < \pi/2$ the solution with the sign + corresponds to point P_3 in figure 2 and the solution with sign – to point P_4. For $-\pi < \beta < -\pi/2 \cup \pi/2 < \beta \leq \pi$ the solution with the sign + corresponds to point P_4, that with sign – to point P_3. After some simplifications, the co-ordinates of points P_3 and P_4 result:

$$\left\{\mathrm{P}_3,\mathrm{P}_4\right\}^{(S)}:\begin{cases}x_{\mathrm{P}_3,\mathrm{P}_4}=\pm r_r\ \cos\beta\\ y_{\mathrm{P}_1,\mathrm{P}_2}=\pm r_r\ \sin\beta\end{cases},\left|\beta\right|\neq\frac{\pi}{2} \tag{9}$$

Finally, the air-gap length $\delta\left(\mathbf{x}_{\mathrm{O}'},\beta,t\right)$ is given by the distance between the intersection points depending on the spatial angle β. The general expression is:

$$\delta\left(\mathbf{x}_{\mathrm{O}'},\beta,t\right)=\sqrt{\left(x_{\mathrm{P}_1,\mathrm{P}_2}-x_{\mathrm{P}_3,\mathrm{P}_4}\right)^2+\left(y_{\mathrm{P}_1,\mathrm{P}_2}-y_{\mathrm{P}_3,\mathrm{P}_4}\right)^2} \tag{10}$$

The closed form of the air-gap length $\delta\left(\mathbf{x}_{\mathrm{O}'},\beta,t\right)$ depends on position of the intersection points with respect to the half-planes determined by y axis. After some algebra, it results:

$$\delta_{rh}\left(\mathbf{x}_{\mathrm{O}'},\beta,t\right)=\left(\begin{array}{l}r_s^2+r_r^2+x_{\mathrm{O}'}^2\cos 2\beta+4x_{\mathrm{O}'}y_{\mathrm{O}'}\cos\beta\sin\beta-y_{\mathrm{O}'}^2\cos 2\beta-\\ -2r_r\left(x_{\mathrm{O}'}\cos\beta+y_{\mathrm{O}'}\sin\beta\right)+\\ +2\left(x_{\mathrm{O}'}+y_{\mathrm{O}'}\tan\beta-r_r\sec\beta\right)\sqrt{\cos^2\beta\left(r_s^2-\left(x_{\mathrm{O}'}\sin\beta-y_{\mathrm{O}'}\cos\beta\right)^2\right)}\end{array}\right)^{1/2} \tag{11}$$

if the spatial angle satisfies the condition $\left|\beta\right|<\pi/2$, otherwise is:

$$\delta_{lt}\left(\mathbf{x}_{\mathrm{O}'},\beta,t\right)=\left(\begin{array}{l}r_s^2+r_r^2+x_{\mathrm{O}'}^2\cos 2\beta+4x_{\mathrm{O}'}y_{\mathrm{O}'}\cos\beta\sin\beta-y_{\mathrm{O}'}^2\cos 2\beta+\\ +2r_r\left(x_{\mathrm{O}'}\cos\beta+y_{\mathrm{O}'}\sin\beta\right)-\\ -2\left(x_{\mathrm{O}'}+y_{\mathrm{O}'}\tan\beta+r_r\sec\beta\right)\sqrt{\cos^2\beta\left(r_s^2-\left(x_{\mathrm{O}'}\sin\beta-y_{\mathrm{O}'}\cos\beta\right)^2\right)}\end{array}\right)^{1/2} \tag{12}$$

if $-\pi<\beta<-\pi/2\cup\pi/2<\beta\leq\pi$.

It is possible to show that the air-gap length $\delta\left(\mathbf{x}_{\mathrm{O}'},\beta,t\right)$ of eqs. (11) and (12) can be estimated by means of the approximated formula given by [16] [17] if the orbit is circular and its centre is concentric with the stator, i.e. $\mathrm{O}''\equiv\mathrm{O}'$.

In order to calculate the radial force due to the UMP acting on a general element *j*-th of the rotor, once that the spatial air-gap length distribution is known with respect to the considered rotor element and the stator, the Maxwell stress tensor is used:

$$\begin{aligned}\sigma_r&=\frac{1}{2\mu_0}\left(B_r^2-B_\theta^2\right)\\ \sigma_\theta&=\frac{1}{\mu_0}B_r B_\theta\end{aligned} \tag{13}$$

where the subscript r indicates the radial component and θ the tangential component, B is the air-gap flux density and μ_0 is the vacuum magnetic permeability. It is generally commonly

accepted that the tangential component is negligible [16] [17]. Therefore, for simplicity it is assumed that $B_\theta = 0$. The magnetic flux $\mathbf{\Phi}_r$ that crosses radially the air-gap is given by:

$$\mathbf{\Phi}_r = \mathbf{M}\,\Lambda \tag{14}$$

where $\mathbf{M}$ is the magnetomotive force produced by the rotor currents (at no-load) of one pole-pair and Λ is the permeance of the magnetic circuit carrying the magnetic flux $\mathbf{\Phi}_r$.

As first approximation, since the permeance of the air-gap is much smaller than the permeance of the rotor and stator iron core, the last is neglected in the calculation of the magnetomotive force $\mathbf{M}$:

$$\mathbf{M} = \frac{\mathbf{\Phi}_r}{\Lambda} = \frac{\mathbf{B}_r \bar{S}}{\frac{\mu_0 \bar{S}}{2\delta}} = \frac{2\mathbf{B}_r \delta}{\mu_0} \tag{15}$$

where $\bar{S}$ is any normal surface crossed by the magnetic flux. This is a common assumption for all rotating machines (see e.g. [4]), moreover large air-gaps support this approximation in slim generators. More detailed considerations for an accurate calculation are reported in [21]. In order to avoid the saturation in the iron teeth, it is necessary to impose the maximum value of the flux density B_r in the range 0.6÷1 T (at no-load), with highest values for large power machines, as that considered in the following. Note that the UMP is acting on the generator also without power generation, it is sufficient that the magnetic field is excited.

The magnetomotive force $\mathbf{M}$ establishing the air-gap magnetic flux $\mathbf{\Phi}_r$ can be expressed as a Fourier series: its first harmonic component has a sinusoidal spatial distribution through the air-gap with period twice the pole pitch $\tau = \pi R / p_p$ and its amplitude is sinusoidally variable during the time, depending on the supply frequency f_s:

$$\mathbf{M}_1(z,t) = \bar{M}_1 \cos\left(\omega t - \frac{\pi z}{\tau}\right) = \bar{M}_1 \cos\left(\omega t - \frac{\pi z}{\frac{\pi R}{p_p}}\right) = \bar{M}_1 \cos\left(\omega t - p_p \frac{z}{R}\right) \tag{16}$$

where $\omega = 2\pi f_s$, z is the distance around the air-gap from a reference point ($z/R = \beta$), R is the mean air-gap radius and p_p the number of pole-pairs. In fact, the mean air-gap length δ is small compared to the mean air-gap radius R, therefore $R \cong r_s \cong r_r$.

By considering for simplicity only the first harmonic component of the magnetomotive force per each pole, the air-gap flux density becomes:

$$\mathbf{B}_r\left(\mathbf{x}_{O'},\beta,t\right)=\mu_0\frac{\mathbf{M}_1\left(\beta,t\right)/2}{\delta\left(\mathbf{x}_{O'},\beta,t\right)}=\mu_0\frac{\bar{M}_1\cos\left(\omega t-p_p\beta\right)/2}{\delta\left(\mathbf{x}_{O'},\beta,t\right)} \tag{17}$$

where the $\delta\left(\mathbf{x}_{O'},\beta,t\right)$ is the actual air-gap length distribution calculated in eqs. (11)-(12). By using eq. (17) in eq. (13), the Maxwell stress becomes:

$$\sigma_r\left(\mathbf{x}_{O'},\beta,t\right)=\frac{B_r^2\left(\mathbf{x}_{O'},\beta,t\right)}{2\,\mu_0}=\mu_0\frac{M_1^2\left(\beta,t\right)}{8\delta^2\left(\mathbf{x}_{O'},\beta,t\right)}=\frac{\mu_0\,\bar{M}_1^2}{8}\frac{\cos^2\left(\omega t-p_p\,\beta\right)}{\delta^2\left(\mathbf{x}_{O'},\beta,t\right)} \tag{18}$$

The resultant forces, due to the UMP, on the considered element *j*-th of the rotor, in horizontal and vertical direction, are finally obtained by integrating Maxwell stress of eq. (18) along the spatial angle:

$$\begin{aligned}&F_{x,UMP}^{(j)}(\mathbf{x}_{O'},t)=\int_0^{2\pi}\sigma_r\left(\mathbf{x}_{O'},\beta,t\right)r_r^{(j)}l^{(j)}\cos\beta d\beta=\\&=\frac{\mu_0\,\bar{M}_1^2}{8}r_r^{(j)}l^{(j)}\left(\int_{-\pi/2}^{\pi/2}\frac{\cos\beta\cos^2\left(\omega t-p_p\,\beta\right)}{\delta_{rh}^2\left(\mathbf{x}_{O'},\beta,t\right)}d\beta+\int_{\pi/2}^{3\pi/2}\frac{\cos\beta\cos^2\left(\omega t-p_p\,\beta\right)}{\delta_{lt}^2\left(\mathbf{x}_{O'},\beta,t\right)}d\beta\right)\end{aligned} \tag{19}$$

$$\begin{aligned}&F_{y,UMP}^{(j)}(\mathbf{x}_{O'},t)=\int_0^{2\pi}\sigma_r\left(\mathbf{x}_{O'},\beta,t\right)r_r^{(j)}l^{(j)}\sin\beta d\beta=\\&=\frac{\mu_0\,\bar{M}_1^2}{8}r_r^{(j)}l^{(j)}\left(\int_{-\pi/2}^{\pi/2}\frac{\sin\beta\cos^2\left(\omega t-p_p\,\beta\right)}{\delta_{rh}^2\left(\mathbf{x}_{O'},\beta,t\right)}d\beta+\int_{\pi/2}^{3\pi/2}\frac{\sin\beta\cos^2\left(\omega t-p_p\,\beta\right)}{\delta_{lt}^2\left(\mathbf{x}_{O'},\beta,t\right)}d\beta\right)\end{aligned} \tag{20}$$

where $r_r^{(j)}$ and $l^{(j)}$ are respectively the radius and the length of the element *j*-th of the rotor. The spatial angle value $|\beta|=\pi/2$ corresponds to the integration extremes, so it could be calculated as limit of the integrals.

3. Experimental dynamical behaviour due to UMP

As mentioned in the introduction, the experimental validation of the proposed model is made indirectly, i.e. the dynamical behaviour of a machine is analyzed and reproduced by means of its model, the excitation systems and by means of the calculated UMP as regards the electromechanical interaction.

The considered machine is one pole-pair, 3000 rpm steam turbo-generator of 400 MW class, the mass is approximately 134000 kg and the length is about 29 m. Contrary to the previous study presented in [21], in which only the generator was considered, in this case the overall machine is taken into account, even if the experimental results of the machine vibration will be shown only for the two bearings of the generator for the sake of brevity.

The rotor is modelled by means of 153 beam elements with 4 d.o.f.s per node and several lumped masses and inertias are added to the nodes in order to take into account the bladed disk stages and the copper bars on the generator and on the exciter (see figure 3). Even if the oil-film forces are not constant and depend, among other causes, on the loads on the bearings, in order to evaluate only the effects of the UMP, they are considered constant and linearized damping and stiffness coefficients are used for the six bearings. The supporting structure is modelled by means of pedestals, i.e. 2 d.o.f.s system per each support. Therefore the overall d.o.f.s of the model are 628. Figure 3 shows also a close-up of the generator, in which the elements that correspond to the active (slotted) part of the generator are highlighted and the positions of some relevant nodes are reported.

The experimental data, obtained by the condition monitoring system of the machine, are relative to a normal operating sequence composed by 3 phases:

phase 1: a run-up from the still condition to the operating speed (3000 rpm);

phase 2: a no-load period, at the operating speed without power production; during this period the magnetic field of the generator is excited;

phase 3: the following period of power production (synchronization) up to the rated power.

The relative shaft vibrations are measured by a couple of proximity probes at ±45° (directions A and B) from the vertical, placed in correspondence of the bearings. These vibration measurements are rotated in order to have vertical and horizontal components. The vibrations of each bearing case are measured by means of vertical and horizontal accelerometers.

The lower part of figure 4 shows the time histories of the rotating speed and of the electrical load. The records last 27 hours and 40 minutes, but the data are not stored with fixed time step and sometimes data are lost or not stored. Phase 1, the run-up, ends at the first vertical dashed line when the operating speed of 3000 rpm is reached, phase 2 is between the two vertical dashed lines and phase 3 starts after the second vertical dashed line when the electrical load increases.

The upper part of figure 4 shows the 1X absolute vibration time history as amplitude 0-pk for bearing #4. Even if an analysis of these records could be interesting by itself - since they show that the vibration amplitude increases without phase changes in correspondence of the maximum electrical load, indicating the heating of the generator due to Joule's effect - for the validation purposes only phase 2, between the end of the run-up (from 7:10:08) and the start of power production (until 7:30:48) is considered. A close-up of phase 2 is shown in figure 5. The limits of this period are indicated by the vertical dashed lines.

Since the overall machine dynamical behaviour is taken into account, the analysis cannot be limited to the synchronous component only. The waterfall plot of the relative vibration in B direction of bearing #5 is shown in figure 6 and, besides to note the crossing of the machine critical speed at

about 1900 rpm, it is interesting to observe the presence of a not negligible 2X component during all the period of observation.

Given that the 2X component is also evident during the run-up of the machine, see figure 6, it can be attributed to the polar stiffness asymmetry that is intrinsic in the design of the generators with one pole-pair. This phenomenon is documented in literature, for instance in [22] [23]. The polar stiffness asymmetry of one pole-pair generator causes a 2X periodic change in the stiffness matrix along a selected direction, which can be implemented in the finite beam model by means of the method presented in [24] or by means of an equivalent 2X excitation that causes the same effect, as shown in [25] and as done in this paper. The 2X vibrational behaviour during phase 2 is shown in the close-up of figure 7.

Even if the condition monitoring system can display other components in the vibration spectrum, it is not possible to extract the numerical data except for united *n*X component, therefore the vibrational behaviour that can be reproduced is limited to 1X+2X.

If the data of phase 2 are considered, unfortunately it is not possible to reconstruct the exact time instant in which the magnetic field excitation is started nor this information was logged. Anyhow, the required time to reach the maximum air-gap flux density lasts generally about 15 to 20 s. During the magnetic field excitation, electrical power is not produced, but at the end the UMP effect is fully present. If the 1X and 2X experimental vibrations, the rotating speed and the electrical load are considered during the no-load period (from 7:10:08 to 7:30:48) as shown in figure 5 and figure 7, the excitation should be occurred after reaching the operating speed of 3000 rpm and before the application of the electrical load. The corresponding 1X and 2X vibrations do not change very much during this period, the phase is practically constant and the amplitude changes only slightly.

The effect of the UMP is instead noticeable on the centreline loci of the journal ($\overrightarrow{O'O''}$ of figure 2) in the bearings #4 and #5 that are shown in figure 8 and figure 9. These curves confirm that the rotor centreline is misaligned with respect to the fixed parts (bearing cases, generator stator, etc.) at the end of the run-up, even if the reference system is not coincident with that used for the simulated absolute response of the rotor. During the no-load period, from 7:10:08 to 7:30:48, the rotor is pulled towards the left-bottom, more appreciably in horizontal than in vertical direction. In bearing #4 the displacements are about 31 μm and 11 μm respectively, in bearing #5 about 56 μm and 21 μm respectively.

The run-up speed transient of phase 1 is used for the calibration of the machine model and to identify the exciting systems, actual or equivalent, that causes the vibrations when the operating speed is reached as explained in the next section. The machine behaviour during the no-load period

is instead used for the validation of the UMP proposed model, since the magnetic field excitation occurs during this period.

4. Validation of the calculation model of the UMP

4.1. Identification of the exciting systems before the magnetic field excitation

Since the proposed method assumes as input the actual machine orbit that is due not only to the UMP forces (these exist only after the magnetic field excitation in the generator), but mainly to the natural unbalance and bow distribution of the machine (excluding any other impending fault), to the gravity and to the generator stiffness asymmetry, therefore the first step is the identification of the external periodic equivalent forces that are the main causes of the machine vibrations before the magnetic field excitation.

Even if the start-up data of phase 1 are not ideal for the identification of the unbalance distribution, since the thermal state of the machine is not stable and the machine model could be in this case not very accurate, it has been decided to find out only a reduced number of exciting forces that equivalently cause the dynamical behaviour of the machine.

As regards the 1X component, for simplicity only two equivalent unbalances are identified, the position of one of which is forced to be on the generator. The identification method, which uses the machine vibration in phase 1, is not reported for the sake of brevity and is fully described in [26] [25].

The identified unbalance on the generator is plausible, resulting $me = 0.3\,\text{kgm} \,@\, \varphi_{umb} = 140°$ on node 114. This force, along with the other one that resulted on the HP turbine (even with a rather high module), causes a simulated vibration of the machine which is very alike to the actual 1X vibration.

As regards the 2X component, the effects of asymmetry on the rotor dynamical behaviour can be reproduced by means of a pair of 2X opposite external moments applied on the extremes nodes of the generator slotted part (nodes 111 and 121 of figure 3), see [25] for further details, which resulted equal to $M_{asy} = 8000\,\text{Nm} \,@\, \varphi_{umb} = 90°$.

4.2. Simulation of the dynamic behaviour of the machine

In order to evaluate the effects of the UMP during the magnetic field excitation, the dynamical behaviour of the considered complete machine is calculated. The general *j*-th rotor element d.o.f.s (generalized displacements, see [25]) are ordered as:

$$\mathbf{x}^{(j)} = \left\{ x_j \quad \vartheta_{x_j} \quad y_j \quad \vartheta_{y_j} \quad x_{j+1} \quad \vartheta_{x_{j+1}} \quad y_{j+1} \quad \vartheta_{y_{j+1}} \right\}^{\mathrm{T}} \tag{21}$$

The fully assembled system (rotor + bearings + foundation) mass matrix - which takes also into account the secondary effect of the rotatory inertia -, the damping matrix, the stiffness matrix - which takes also into account the shear effect - and the gyroscopic matrix can be defined by means of standard Lagrange's methods for beam elements as shown e.g. in [27], while the assembly of the total system (rotor, bearings and supporting structure) equations can be done by following the method described in [25]:

$$[\mathbf{M}]\ddot{\mathbf{x}} + [\mathbf{C}]\dot{\mathbf{x}} + [\mathbf{K}]\mathbf{x} = \mathbf{F}(\mathbf{x}, t) + \mathbf{W} \tag{22}$$

where $[\mathbf{M}]$ is the mass matrix, $[\mathbf{C}]$ is the damping matrix, which includes also the gyroscopic matrix calculated at the operating speed Ω, $[\mathbf{K}]$ is the stiffness matrix and $\mathbf{W}$ the weight.

The external exciting force vector $\mathbf{F}(\mathbf{x}, t)$ of eq. (22) includes the original unbalance of the rotor, the equivalent 2X bending moments on the generator and the effect of the UMP (only if the magnetic field is excited). Moreover, the UMP acting on a rotor element, is applied into the first node of the element (figure 10), even if it is calculated using the element span, see eqs. (19) and (20).

The structure of the column vector $\mathbf{F}(\mathbf{x}, t)$ is typically:

$$\begin{aligned}
&\mathbf{F}(\mathbf{x}, t) = \mathbf{F}_{unb}(t) + \mathbf{F}_{asy}(t) + \mathbf{F}_{UMP}(\mathbf{x}, t) \\
&\mathbf{F}_{unb}(t) = \left\{ \vdots \quad \underbrace{m e \Omega^2 \cos\left(\Omega t + \varphi_{unb}\right) \quad 0 \quad m e \Omega^2 \sin\left(\Omega t + \varphi_{unb}\right) \quad 0}_{\text{rotor node in which the unbalance is applied}} \quad \vdots \quad \underbrace{0 \quad \cdots \quad 0}_{\text{foundation d.o.f.s}} \right\}^{\mathrm{T}} \\
&\mathbf{F}_{asy}(t) = \left\{ \begin{array}{l} \vdots \quad \underbrace{0 \quad M_{asy} \cos\left(2\Omega t + \varphi_{asy}\right) \quad 0 \quad M_{asy} \sin\left(2\Omega t + \varphi_{asy}\right)}_{\text{first node of the generator slotted part}} \quad \vdots \\ \vdots \quad \underbrace{0 \quad -M_{asy} \cos\left(2\Omega t + \varphi_{asy}\right) \quad 0 \quad -M_{asy} \sin\left(2\Omega t + \varphi_{asy}\right)}_{\text{last node of the generator slotted part}} \quad \vdots \quad \underbrace{0 \quad \cdots \quad 0}_{\text{foundation d.o.f.s}} \end{array} \right\}^{\mathrm{T}} \\
&\mathbf{F}_{UMP}(\mathbf{x}, t) = \left\{ \vdots \quad \underbrace{F_{x,UMP}^{(k)} \quad 0 \quad F_{y,UMP}^{(k)} \quad 0}_{\substack{\text{first node of } k\text{-th element in which} \\ \text{the UMP is applied}}} \quad \vdots \quad \underbrace{0 \quad \cdots \quad 0}_{\text{foundation d.o.f.s}} \right\}^{\mathrm{T}}
\end{aligned} \tag{23}$$

If the node of application of a force in eq. (23) coincides with the application node of another type of force, then superposition of the two effects is used.

The non-linear system of equations in eq. (22) is integrated in the time domain using the Newmark implicit method, in which the forcing vector of eq. (23) is recalculated at each time step: the UMP

forces are calculated using eqs. (19) and (20) considering the air-gap distribution due to the vibration at the previous time step.

4.3. Machine response before the magnetic field excitation

Anyhow the actual difficulty is to determine the initial conditions $\mathbf{x}_0$ and $\dot{\mathbf{x}}_0$ to be used in the Newmark algorithm. In order to find them and to have a confirmation that the model can reproduce the dynamical behaviour of the actual machine, the steady state response of the machine at 3000 rpm before the magnetic field excitation is calculated by integrating eq. (22) and neglecting $\mathbf{F}_{UMP}(\mathbf{x},t)$. Using a time step of 1e−4 s, which corresponds to 200 points per each orbit at 3000 rpm, even setting null vectors for $\mathbf{x}_0$ and $\dot{\mathbf{x}}_0$, the steady state response is reached after few seconds of simulation. If the machine model and the identified excitation system are satisfactory, the simulated dynamical response of the machine should reproduce the experimental one, once the machine has reached the operating speed, i.e. at 7:10:08 of the time scale. Figure 11 shows some superposed rotor direct orbits in bearing #4 once the operating speed is reached and immediately after (thus the time indicated is 7:10:48). Since the considered model is able to reproduce only the 1X and 2X behaviour, the corresponding experimental filtered orbits in bearing #4 are shown in figure 12 and figure 13 at 7:10:08. If these are compared to the simulated results without the magnetic field excitation, shown in figure 14, the agreement is good and also the overall simulated response (1X+2X in figure 14) fits the shape and the dimensions of the direct experimental response of figure 11, except for some noise.

If bearing #5 is considered, similar results are obtained. Note that experimental orbits are always centred in the origin of reference system S'' (see figure 2) due to the internal conventions of the condition monitoring system, while the simulated ones are referred to the reference system S'.

The overall good results obtained with the simulation of the machine dynamical behaviour before the magnetic field excitation allows considering the model of the machine and the identified equivalent excitations as reliable.

4.4. Effect of the UMP due to the magnetic field excitation during the transient

Starting from the dynamical behaviour of the machine reproduced by the calibrated model, the effect of the UMP is now considered. As shown in figure 14, the orbit of the rotor before the magnetic field excitation is misaligned with respect to the ideal stator centreline, resulting from the dynamic deformation, the effect of the weight and the oil-film forces. Therefore the air-gap distribution in correspondence of the rotor elements on the active part of the generator is not radially symmetric.

The transient dynamical behaviour of the machine due to the gradual excitation of the magnetic field in the air-gap is simulated in the present section. As already said, the maximum air-gap magnetic flux on generators of the considered class is reached in 15-20 s. The flux density increasing is practically linear in real machines and in this paper it is assumed that passes from 0 to 1 T linearly in 15 s.

The overall simulation lasts 20 s with a time step of 1e–4 s, while the initial conditions $\mathbf{x}_0$ and $\dot{\mathbf{x}}_0$ for $t = 0$ are taken from the calculation of the steady-state of the dynamical response without magnetic field excitation. Therefore the simulation represent the transient of phase 2: the machine is at the operating speed without the magnetic field excitation, the field is then linearly excited up to the maximum value of the flux density and finally the machine reaches a new steady state during the last 5 s. Eq. (22) is therefore integrated considering also the term $\mathbf{F}_{UMP}(\mathbf{x},t)$. Since the simulation results per each d.o.f. is composed by 2e5 values, it is not very useful to plot all the orbits together, while it is useful to analyze the dynamical behaviour just after exciting the magnetic field and its evolution with a time step of 1 s.

Figure 15 shows the rotor orbits during the first second for bearing #4. The previous steady state orbits (dashed lines in the figures) are notably modified, the behaviour tends to become chaotic and the rotor starts to move towards the minimum air-gap length. It is also possible to note in figure 15 when the rotor centre leaves the steady state orbit as a consequence of the incipient UMP.

Figure 16 shows the evolution of the dynamical behaviour of the rotor by plotting only one orbit with a step of 1 s. It is possible to observe the increasing of the rotor eccentricity that grows non-linearly until the maximum value of the air-gap flux is reached. Afterwards the rotor orbits reach quickly a new steady state as shown by those corresponding to 15-20 s. Moreover, even if the rotor orbits are rather deformed just after the beginning of the magnetic field excitation (see the orbits corresponding to the first seconds of simulation and figure 15), the orbits of the new steady state are similar to those of the former one. Similar results are obtained also for bearing #5.

These qualitative observations indicate that the dynamical behaviour simulated by the model is corresponding to that of the experimental one of the machine: apparently, after the transient, the orbit shapes are very similar to the initial ones (therefore the 1X and 2X components have not sensibly changed) but they are shifted as the centreline loci in figure 8 and figure 9. The quantitative evaluation is made by considering the two steady state vibration spectra in bearing #4, that are shown in figure 17 and figure 18. No meaningful differences in the 1X and 2X amplitudes can be observed, but at the end of the transient the spectra have several components also at higher frequencies with 50 Hz sidebands, which can be ascribed to non-linear effects. Anyhow these

components have vanishing small amplitudes, below the practical possibility to measure them. The results are similar for bearing #5.

This is confirmed by the data in table 1 and table 2 that compare experimental time histories with simulated results: 1X and 2X vibrations are practically unchanged, while the displacements of the average position of the shaft are close to the actual centreline shifts in figure 8 and figure 9. In bearing #4 centreline displacements are about 35.97 μm in horizontal and 14.03 μm in vertical direction, in bearing #5 about 61.26 μm and 21.68 μm respectively.

Due to the good agreement between the experimental dynamical behaviour and the simulated one by means of the proposed model, it is possible to consider the model as validated.

Since the dynamical behaviour has been simulated for the complete machine, it is also possible to evaluate the effect of the application of the magnetic field on the generator also on the nodes that do not correspond to the experimental measuring planes: figure 19 shows the average dynamical deformation and the orbits of the generator nodes after and before the excitation of the magnetic field in the air-gap. The displacement due to the UMP is clearly recognizable.

A further important result is that the validated model allows the calculation of the UMP forces on all the nodes of the active part of the generator and it is interesting to analyze the values obtained both during the transient and the steady state.

The analysis of the forces during the transient is made by considering the calculated values of $\mathbf{F}_{UMP}(\mathbf{x},t)$ and analyzing them by means of short time Fourier transform (STFT). In order to have a good frequency resolution, Hamming windowing of 2^{14} samples with 2^{13} overlapping is used, while the integration step equal to 1e–4 s implies the sampling frequency of 10 kHz and the maximum bandwidth of 5 kHz. Figure 20 shows the spectrogram obtained for the UMP force in vertical direction in node 116, which corresponds to mid-span of the generator. As regards the time domain analysis, it is possible to observe that there is the presence of several components that tends to increase during the magnetic field excitation, but when the air-gap flux has reached its maximum value after 15 s of simulation, a discontinuity is evident. Only few harmonic components are always present. There is a family at high frequency, close to 1.4 kHz and also 1X and 2X components are clearly observable. Other components tend to rapidly disappear after the discontinuity. Spectrograms for the UMP forces applied in other nodes and directions indicate similar results.

A more precise analysis in the frequency domain is possible by considering the UMP force spectrum at the end of the transient, once the steady state is reached. Figure 21 shows the UMP vertical force spectrum in node 111, limited to 1.6 kHz. Some components are clearly recognizable: 1X and 2X components are evident as also a family of not integer multiple of rotation frequency, but with sidebands spaced with the rotation frequency, at about 1.4 kHz. These last force

components can be ascribed to non-linear effects due to electromechanical interaction. If the force amplitudes are considered, the average force (static) is largely predominant, being an order of magnitude greater than 1X component. Also high frequency components are not negligible and some are greater than the 2X component. The results, not shown for brevity, are similar in the other nodes of the active part of the generator and for both horizontal and vertical direction.

The evaluation of the force magnitudes, in which the static component is predominant, allows explaining both the experimental and simulated dynamical behaviour in which the most evident effect is on the rotor offset. The horizontal and vertical resultants are respectively 45610 N and 91880 N that have to be compared with the weight of the generator alone that is nearly 600000 N. Bearings are less stiff in horizontal direction, so that the horizontal offset is greater.

A final remark can be done by comparing the results obtained by the validated model with other simplified model proposed in literature. Normally UMP effect is believed to cause only a static and a 2X force component. This is confirmed by this study, but the 2X effect is very small indeed and, in case of one pole-pair generators, masked by the dynamical effect of the polar stiffness asymmetry. This study has shown that also a 1X force component, the effect of which is overwhelmed by the unbalance, and strong non-linear effects are present.

5. Conclusions

An accurate analysis of the dynamical phenomena related to electromechanical interaction in slim generators is possible by means of the model proposed in the paper. The forces due to unbalanced magnetic pull are calculated by means of a method that takes into consideration the actual orbit of the rotor centre in the time, for all the elements of the generator active part. The rotor-dynamics aspect is carefully considered by means of the complete model of the machine, in which the rotor is modelled by means of finite elements, the bearing effects by stiffness and damping coefficients and the foundation by pedestals. The model based simulation, using the “normal” exciting systems acting on the rotor and the unbalanced magnetic pull, is able to correctly reproduce the dynamical behaviour of real machines. The validation of the method is presented by analyzing in detail an experimental case of a steam turbo-generator, that allowed the effects of the unbalanced magnetic pull to be highlighted.

References

[1] Bradford, M. (1968): Unbalanced magnetic pull in a 6-pole induction motor. *Proc. IEE*, **115**(11), pp. 1619-1627.

[2] Binns, K.J. and Dye, M. (1973): Identification of principal factors causing unbalanced magnetic pull in cage induction motor. *Proc. IEE*, **120**(3), pp. 349-354

[3] Dorrel, D.G. and Smith, A.C. (1994): Calculation of U.M.P. in induction motors with series or parallel winding connections. *IEEE Transactions on Energy Conversion*, **9**(2), pp. 304-310.

[4] Smith, A.C. and Dorrel, D.G. (1996): Calculation and measurement of unbalanced magnetic pull in cage induction motors with eccentric rotors. Part 1: Analytical model. *IEE Proc.-Electr. Power Appl.*, **143**(3), pp. 193-201.

[5] Dorrel, D.G. (1996): Calculation of unbalanced magnetic pull in small cage induction motors with skewed rotors and dynamic rotor eccentricity. *IEEE Transactions on Energy Conversion*, **11**(3), pp. 483-488.

[6] Smith, A.C. and Dorrel, D.G. (1996): Calculation and measurement of unbalanced magnetic pull in cage induction motors with eccentric rotors. Part 2: Experimental investigation. *IEE Proc.-Electr. Power Appl.*, **143**(3), pp. 202-210.

[7] Dorrel, D.G., Thomson, W.T. and Roach, S. (1997): Analysis of airgap flux, current, and vibration signals as a function of the combination of static and dynamic airgap eccentricity in 3-phase induction motors. *IEEE Transactions on Industry Applications*, **33**(1), pp. 24-34.

[8] Dorrel, D.G. (1999): Experimental behaviour of unbalanced magnetic pull in 3-phase induction motors with eccentric rotors and the relationship with tooth saturation. *IEEE Transactions on Energy Conversion*, **14**(3), pp. 304-309.

[9] Belmans, R., Vandenput, A. and Geysen, W. (1987): Influence of unbalanced magnetic pull on the radial stability of flexible-shaft induction machines. *IEE Proceedings Part B*, **134**(2), pp. 101-109.

[10] Holopainen, T.P., Tenhunen, A. and Arkkio, A. (2005): Electromechanical interaction in rotordynamics of cage induction motors. *Journal of Sound and Vibration*, **284,** pp. 733-755.

[11] Tenhunen, A., Benedetti, T., Holopainen, T.P. and Arkkio, A. (2003): Electromagnetic forces of the cage rotor in conical whirling motion. *IEE Proceedings - Electric Power Applications*, 150(5), pp. 563-568.

[12] Holopainen, T.P., Tenhunen, A., Lantto, E. and Arkkio, A. (2005): Unbalanced magnetic pull induced by arbitrary eccentric motion of cage rotor in transient operation. Part 1: Analytical model. *Electrical Engineering*, 88(1), pp. 13-24.

[13] Holopainen, T.P., Tenhunen, A., Lantto, E. and Arkkio, A. (2005): Unbalanced magnetic pull induced by arbitrary eccentric motion of cage rotor in transient operation. Part 2: Verification and numerical parameter estimation. *Electrical Engineering*, 88(1), pp. 25-34.

[14] Holopainen, T.P., Tenhunen, A., Lantto, E. and Arkkio, A. (2004): Numerical identification of electromagnetic force parameters for linearized rotordynamic model of cage induction motors. *Journal of Vibration and Acoustics, Transactions of the ASME*, 126(3), pp. 384-390.

[15] Zawoysky, R.J. and Tornroos, K.C. (2001): GE generator rotor design, operational issues and refurbishment options. *GE power System Report*, GER 4212, 08/01, pp. 1-28.

[16] Stoll, R.L. (1997): Simple computational model for calculation the unbalanced magnetic pull on a two-pole turbogenerator rotor due to eccentricity. *IEE Proc.-Electr. Power Appl.*, **144**(4), pp. 263-270.

[17] Guo, D., Chu, F. and Chen, D. (2002): The Unbalanced Magnetic Pull and its Effects on Vibration in a Three-Phase Generator with Eccentric Rotor. *Journal of sound and Vibration*, **254**(2), pp. 297-312.

[18] Nabil, A.A.N. and Toliyat, H.A. (1998): A novel method for modeling dynamic air-gap eccentricity in synchronous machines based on modified winding function theory. *IEEE*

Transactions on Energy Conversion, **13**(2), pp. 156-162.

[19] Toliyat, H.A. and Nabil, A.A.N. (1999): Simulation and detection of dynamic air-gap eccentricity in salient-pole synchronous machines. *IEEE Transactions on Industry Applications*, **35**(1), pp. 86-93.

[20] Gustavsson, R.K. and Aidanpää J.-O. (2004): The influence of Magnetic Pull on the Stability of Generator Rotors. Proc. of *The 10th Intl. Symposium on Transport Phenomena and Dynamics of Rotating Machinery*, Honolulu, Hawaii, March 7-11, pp. 1-9.

[21] Pennacchi, P. and Frosini, L. (2005): Dynamical Behaviour of a Three-Phase Generator Due to Unbalanced Magnetic Pull. *IEE Proc. Electric Power Applications*, **152**(6), pp. 1389-1400.

[22] Bachschmid, N. and Diana, G. (1980): Reduction of twice per revolution vibration levels due to weight effect in large turbogenerators. Proc. of *IMechE Second International Conference Vibration in Rotating Machinery*, Churchill College, Cambridge, 2-4 Sept., pp. 203-208.

[23] Bachschmid, N. and Frigeri, C. (1982): Some results on the twice-per-revolution balancing of generators. Proc. of *IFToMM International Conference Rotordynamic Problems in Power Plants*, Rome, 28 Sept.-1 Oct., pp. 49-54.

[24] Genta, G. (1998): Whirling of unsymmetrical rotors A finite element approach based on complex coordinates. *Journal of Sound and Vibration*, **124**(1), pp. 27-53.

[25] Pennacchi, P., Bachschmid, N., Vania, A., Zanetta, G.A. and Gregori, L. (2006): Use of modal representation for the supporting structure in model based fault identification of large rotating machinery: part 1 – theoretical remarks. *Mechanical Systems and Signal Processing*, **20**(3), pp. 662-681.

[26] Bachschmid, N., Pennacchi, P. and Vania, A. (2002): Identification of multiple faults in rotor systems. *Journal of Sound and Vibration*, **254**(2), pp. 327–366.

[27] Lalanne, M. and Ferraris, G. (1988): Rotordynamics Prediction in Engineering. John Wiley & Sons Inc, Chichester, England.

Figure captions

Figure 1: Air-gap distribution along the rotor.

Figure 2: Calculation of the air-gap length $\delta(\mathbf{x}_{O'}, \beta, t)$.

Figure 3: Finite beam model of the considered machine and particular of the generator.

Figure 4: Time history of the 1X vibrations measured in bearing #4 during the complete period of the machine operation and corresponding rotating speed and electrical load.

Figure 5: Close-up of the time history of 1X vibrations measured in bearing #4 during the considered period of the machine operation and corresponding rotating speed and electrical load.

Figure 6: Waterfall plot of the relative vibration in bearing #5, B direction.

Figure 7: Close-up of the time history of 2X vibrations measured in bearing #4 during the considered period of the machine operation and corresponding rotating speed and electrical load.

Figure 8: Centreline locus of the rotor journal in bearing #4.

Figure 9: Centreline locus of the rotor journal in bearing #5.

Figure 10: UMP on a generator element.

Figure 11: Direct rotor orbits in bearing #4 before the magnetic field excitation.

Figure 12: 1X filtered rotor orbit in bearing #4 before the magnetic field excitation.

Figure 13: 2X filtered rotor orbit in bearing #4 before the magnetic field excitation.

Figure 14: Simulated rotor orbits in bearing #4 before the magnetic field excitation.

Figure 15: Simulated transient in bearing #4 during the first second of the magnetic field excitation (dashed line: steady state orbit before excitation, solid line: orbit after excitation).

Figure 16: Simulated transient in bearing #4 during the magnetic field excitation.

Figure 17: Vibration spectrum after and before the magnetic field excitation, bearing #4, horizontal direction.

Figure 18: Vibration spectrum after and before the magnetic field excitation, bearing #4, vertical direction.

Figure 19: Dynamical behaviour of the generator (dashed line: steady state before excitation, solid line: steady state after excitation).

Figure 20: Spectrogram of UMP vertical force in node 116 (mid-span of the generator).

Figure 21: UMP vertical force spectrum in node 111.

Table captions

Table 1: Comparison between experimental data and simulation results, node 100 – Bearing #4 (Note that experimental orbits are always centred in the origin of reference system S'' (see figure 2) due to the internal conventions of the condition monitoring system, while the simulated ones are referred to S').

Table 2: Comparison between experimental data and simulation results, node 133 – Bearing #5 (Note that experimental orbits are always centred in the origin of reference system S'' (see figure 2) due to the internal conventions of the condition monitoring system, while the simulated ones are referred to S').

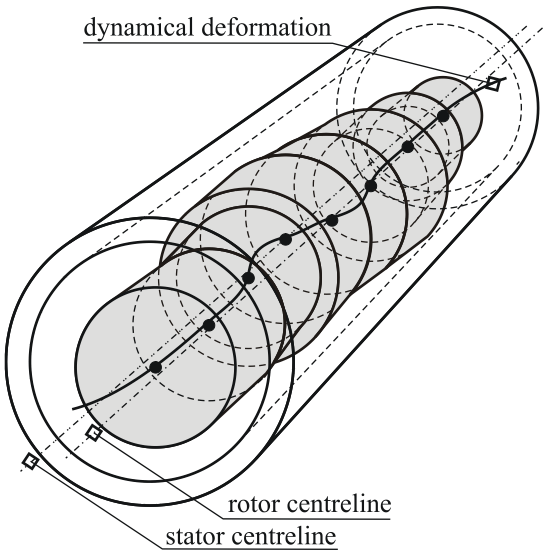

Figure 1: Air-gap distribution along the rotor.

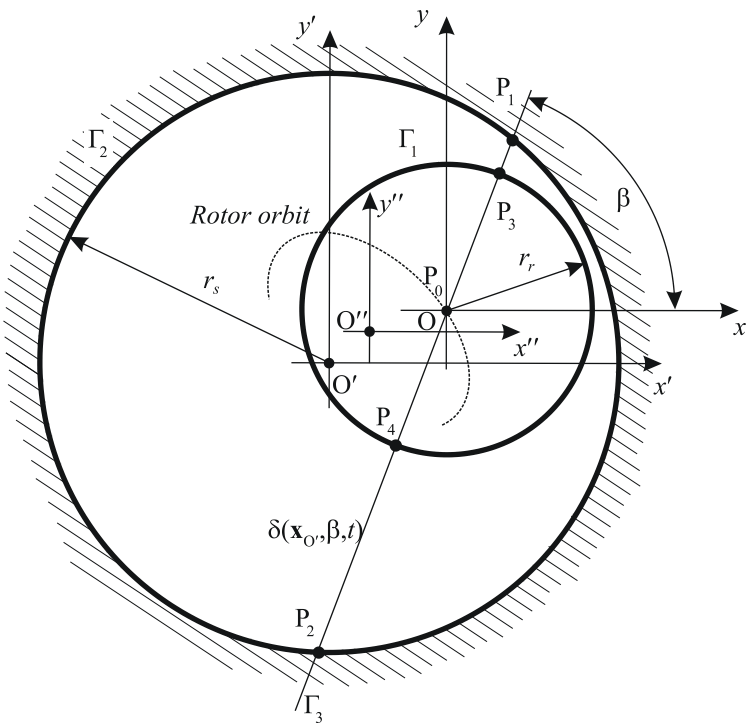

Figure 2: Calculation of the air-gap length $\delta\left(\mathbf{x}_{O'}, \beta, t\right)$.

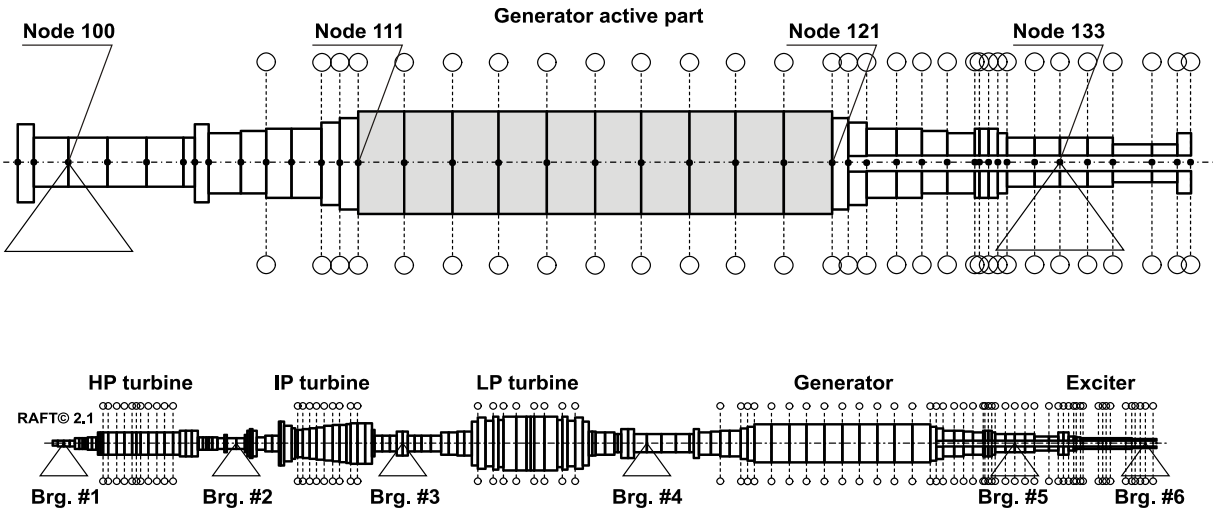

Figure 3: Finite beam model of the considered machine and particular of the generator.

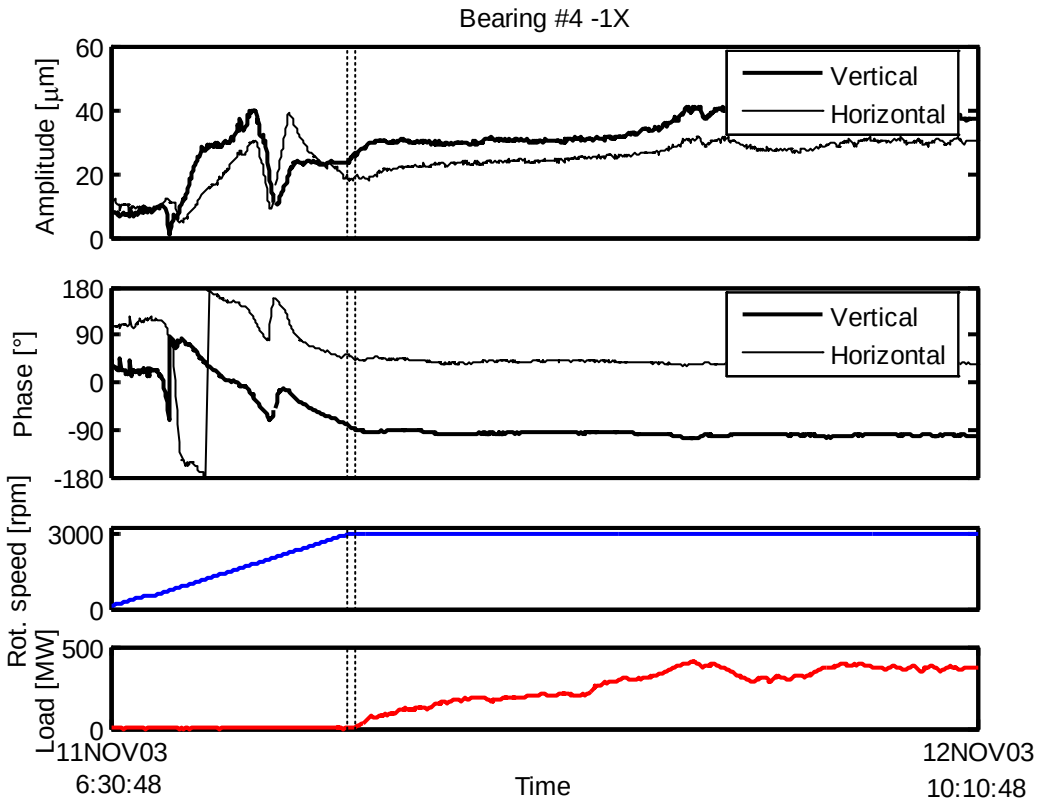

Figure 4: Time history of the 1X vibrations measured in bearing #4 during the complete period of the machine operation and corresponding rotating speed and electrical load.

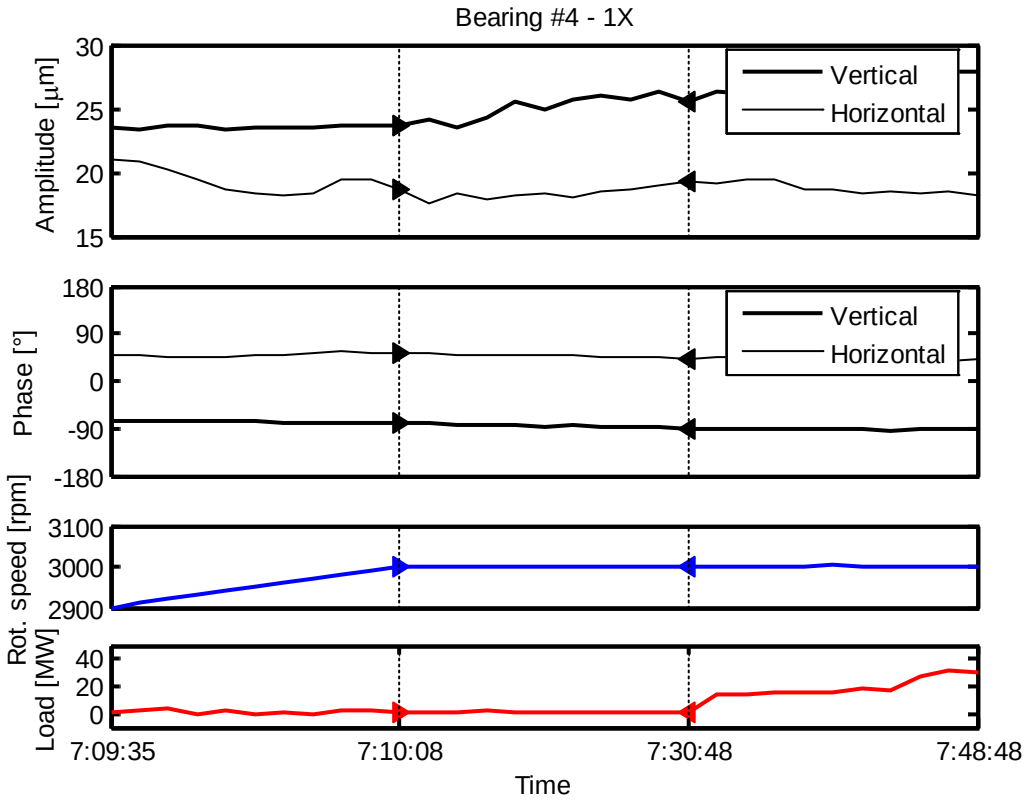

Figure 5: Close-up of the time history of 1X vibrations measured in bearing #4 during the considered period of the machine operation and corresponding rotating speed and electrical load.

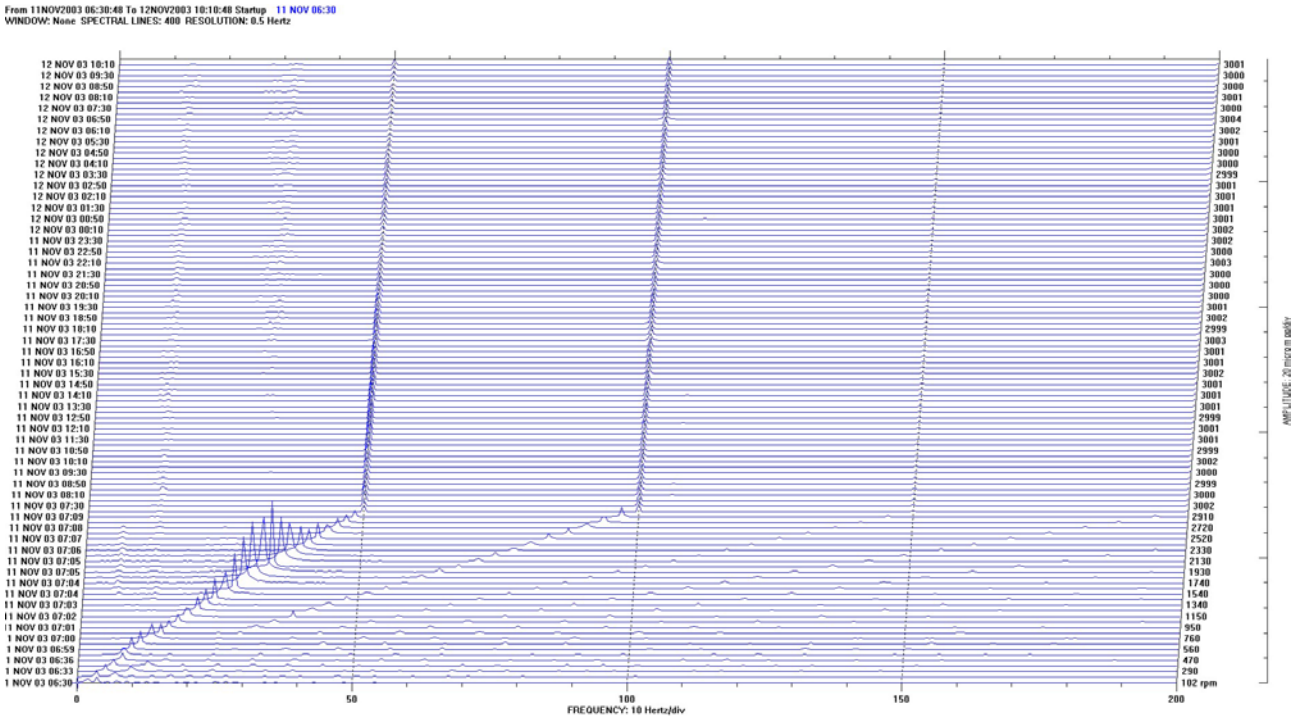

Figure 6: Waterfall plot of the relative vibration in bearing #5, B direction.

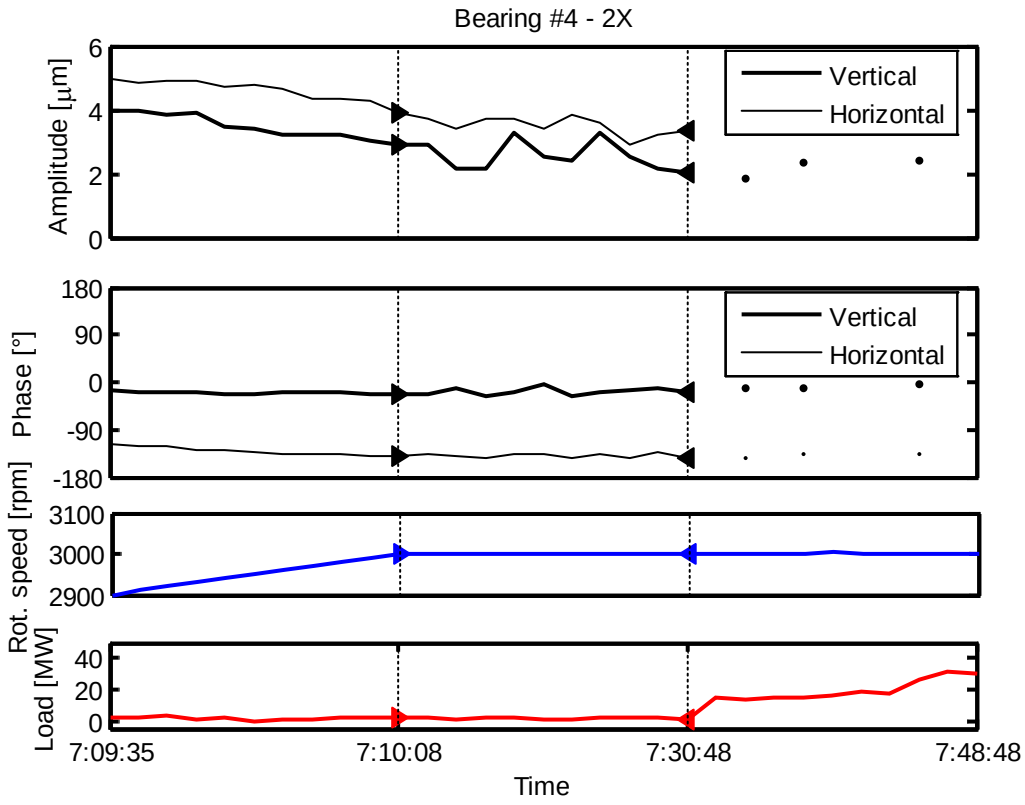

Figure 7: Close-up of the time history of 2X vibrations measured in bearing #4 during the considered period of the machine operation and corresponding rotating speed and electrical load.

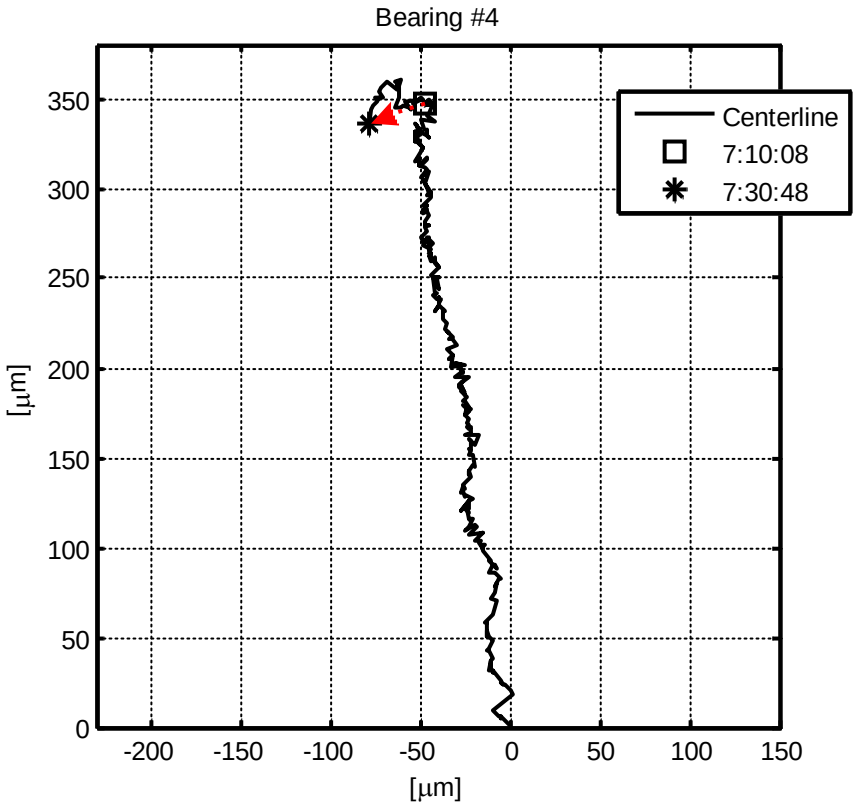

Figure 8: Centreline locus of the rotor journal in bearing #4.

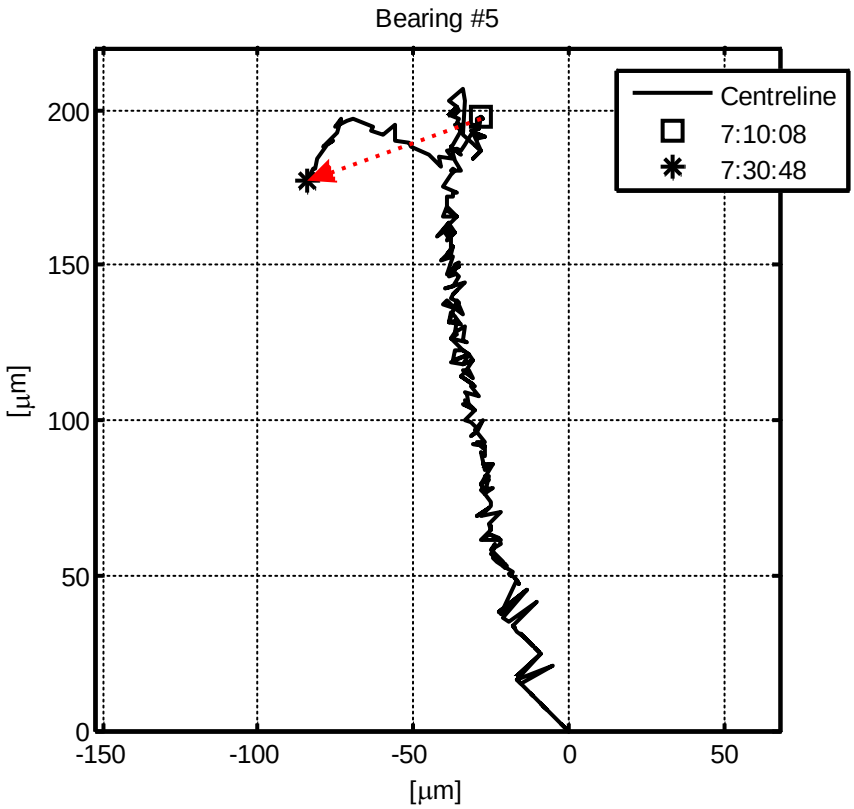

Figure 9: Centreline locus of the rotor journal in bearing #5.

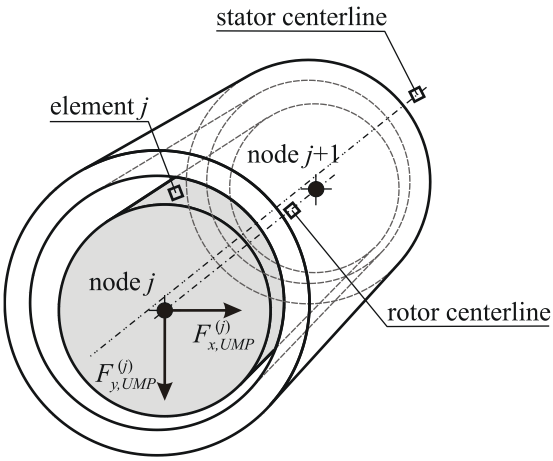

Figure 10: UMP on a generator element.

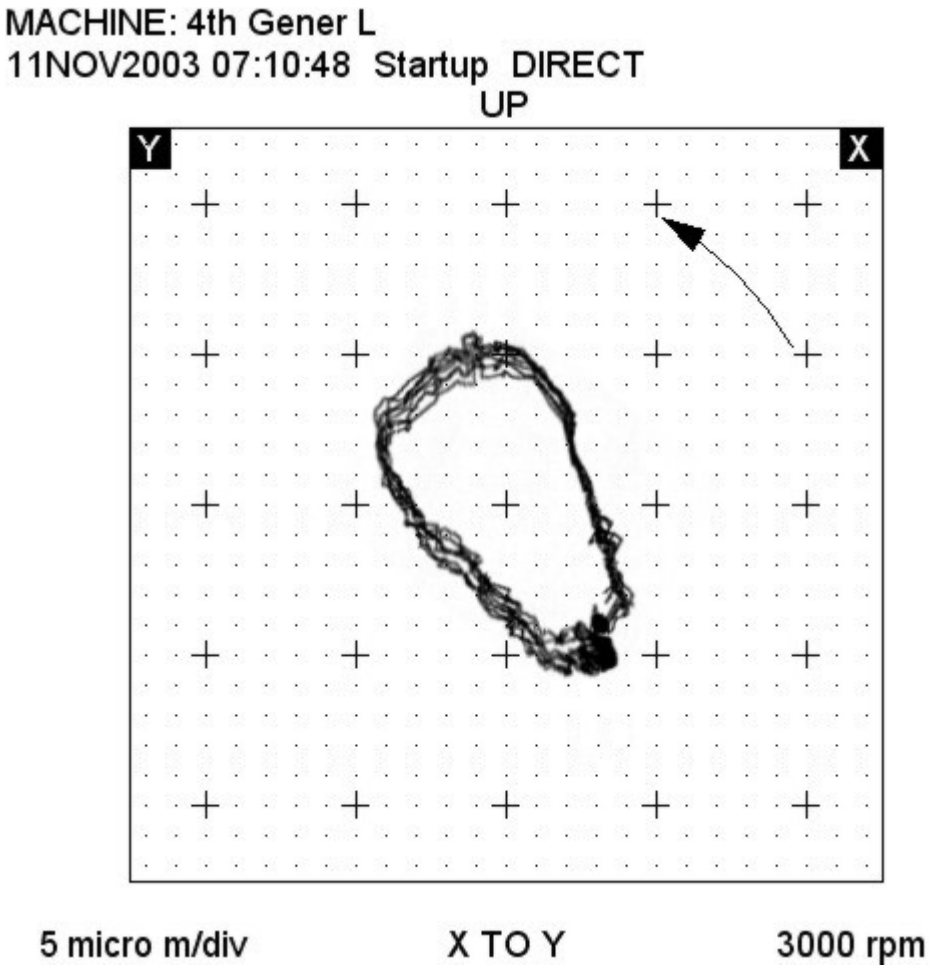

Figure 11: Direct rotor orbits in bearing #4 before the magnetic field excitation.

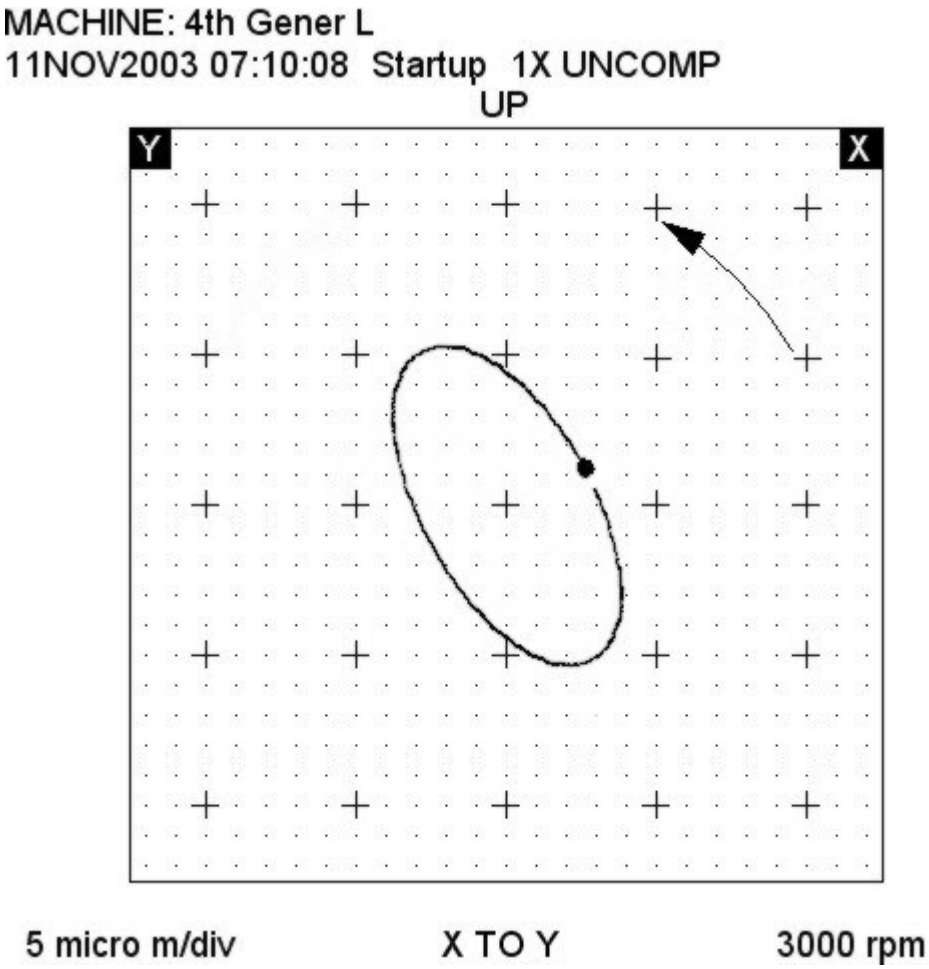

Figure 12: 1X filtered rotor orbit in bearing #4 before the magnetic field excitation.

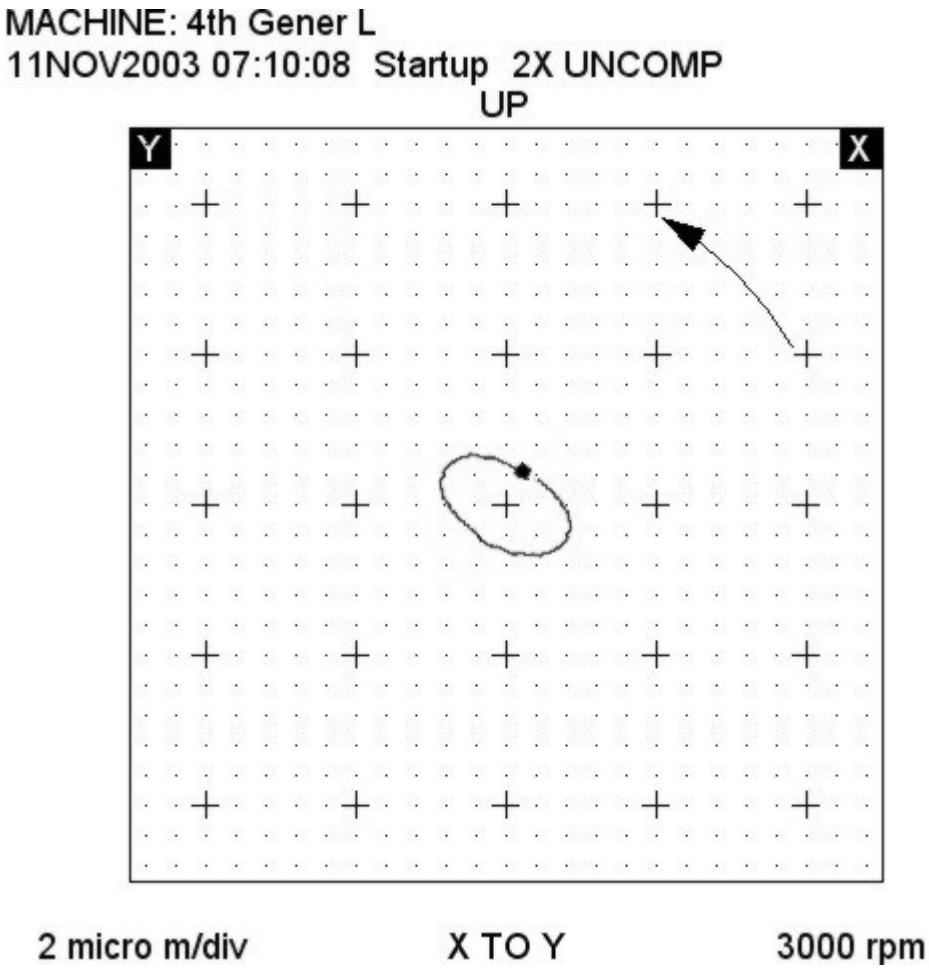

Figure 13: 2X filtered rotor orbit in bearing #4 before the magnetic field excitation.

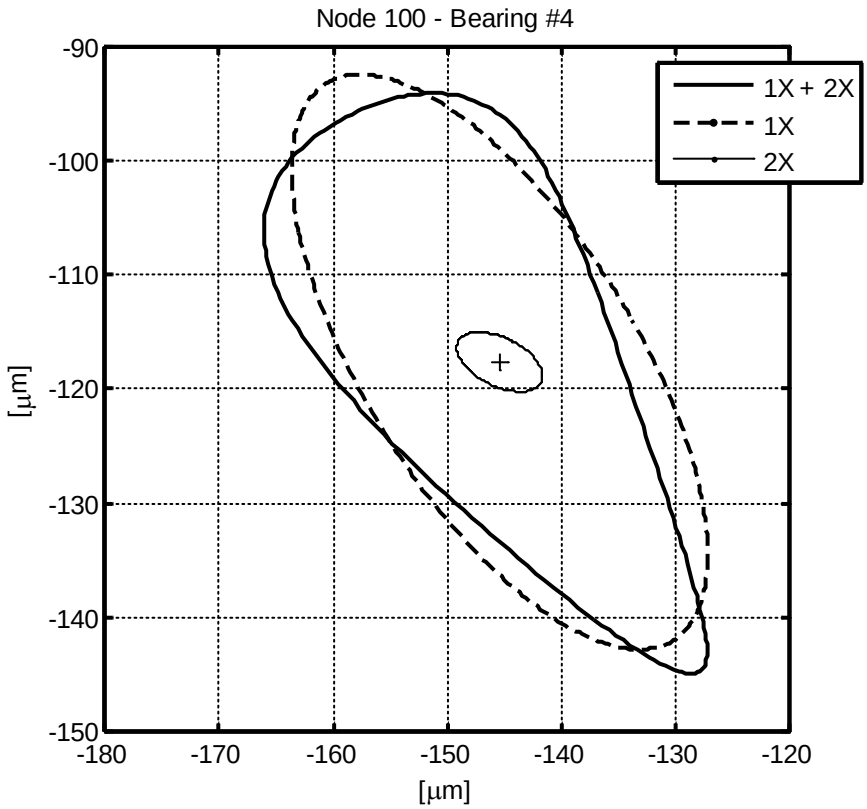

Figure 14: Simulated rotor orbits in bearing #4 before the magnetic field excitation.

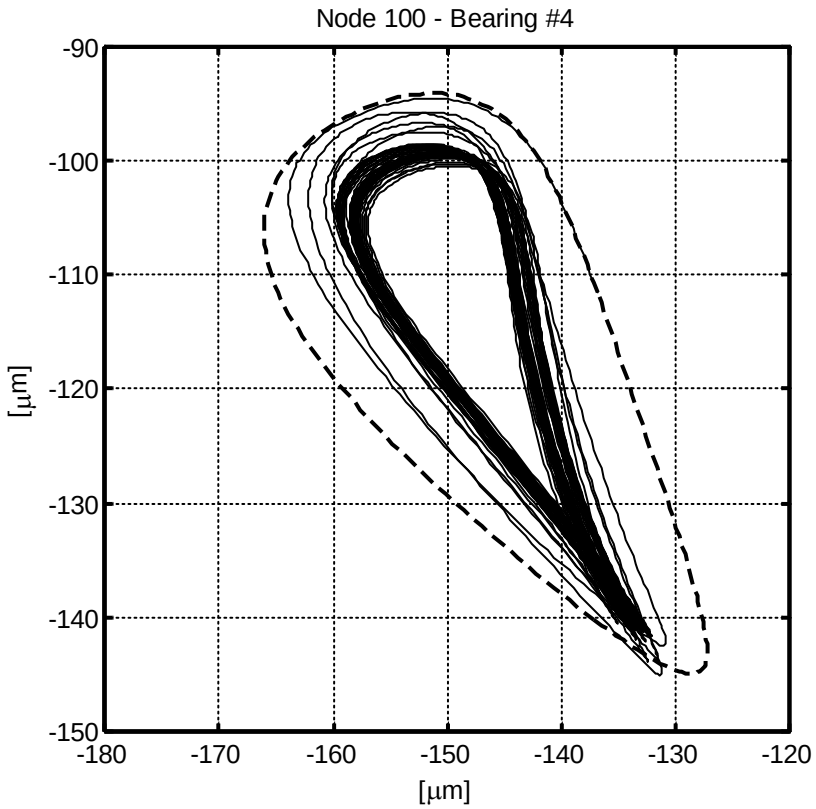

Figure 15: Simulated transient in bearing #4 during the first second of the magnetic field excitation (dashed line: steady state orbit before excitation, solid line: orbit after excitation).

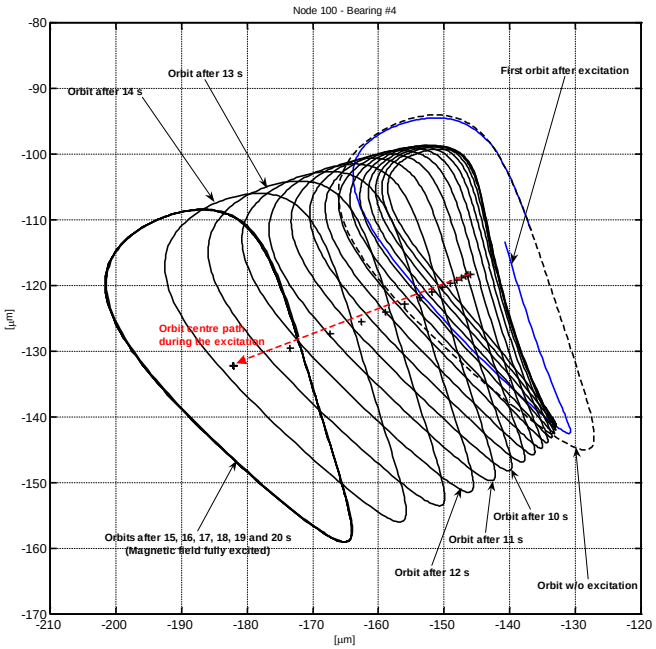

Figure 16: Simulated transient in bearing #4 during the magnetic field excitation.

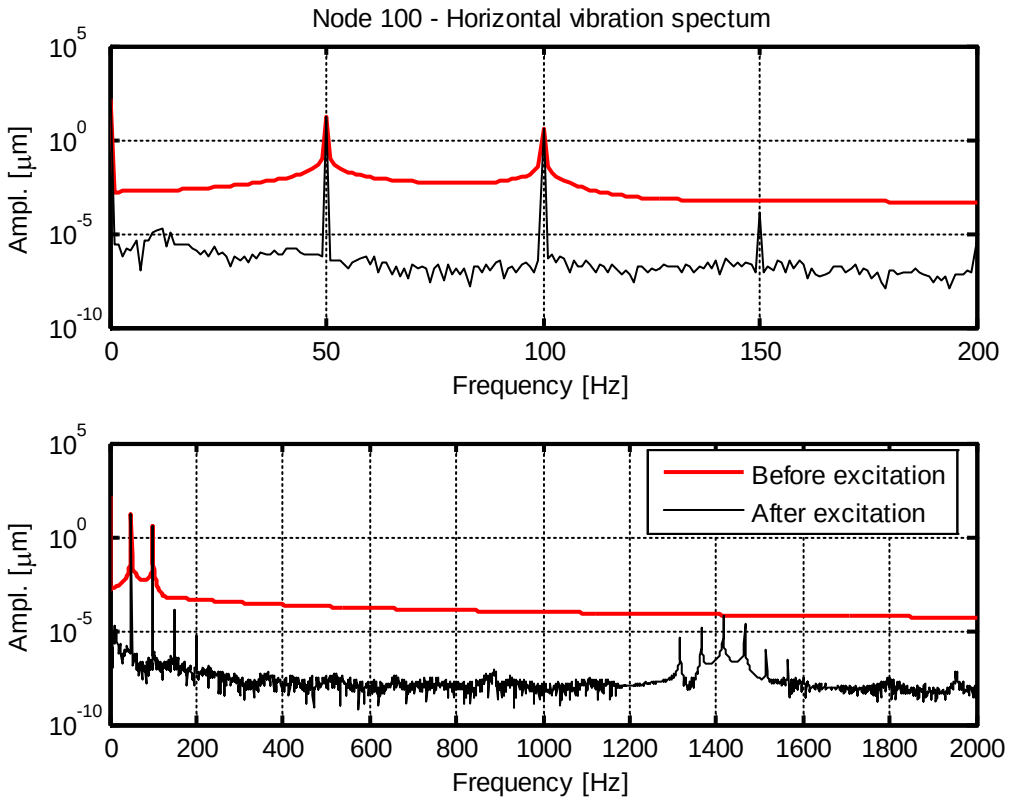

Figure 17: Vibration spectrum after and before the magnetic field excitation, bearing #4, horizontal direction.

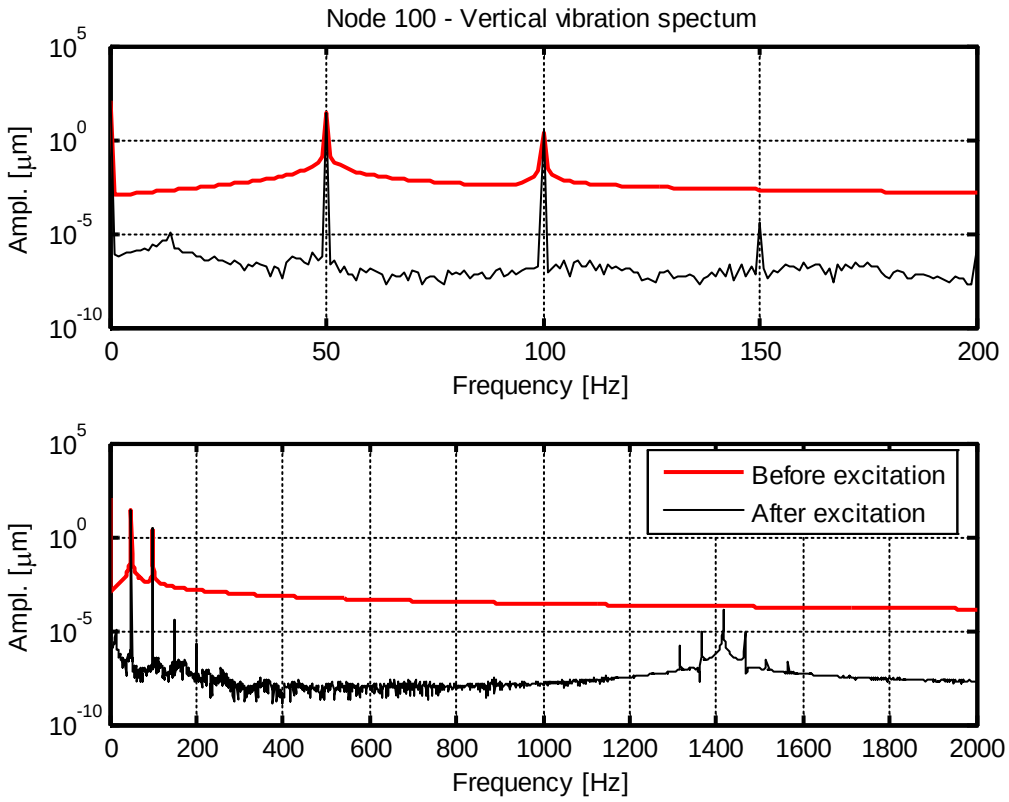

Figure 18: Vibration spectrum after and before the magnetic field excitation, bearing #4, vertical direction.

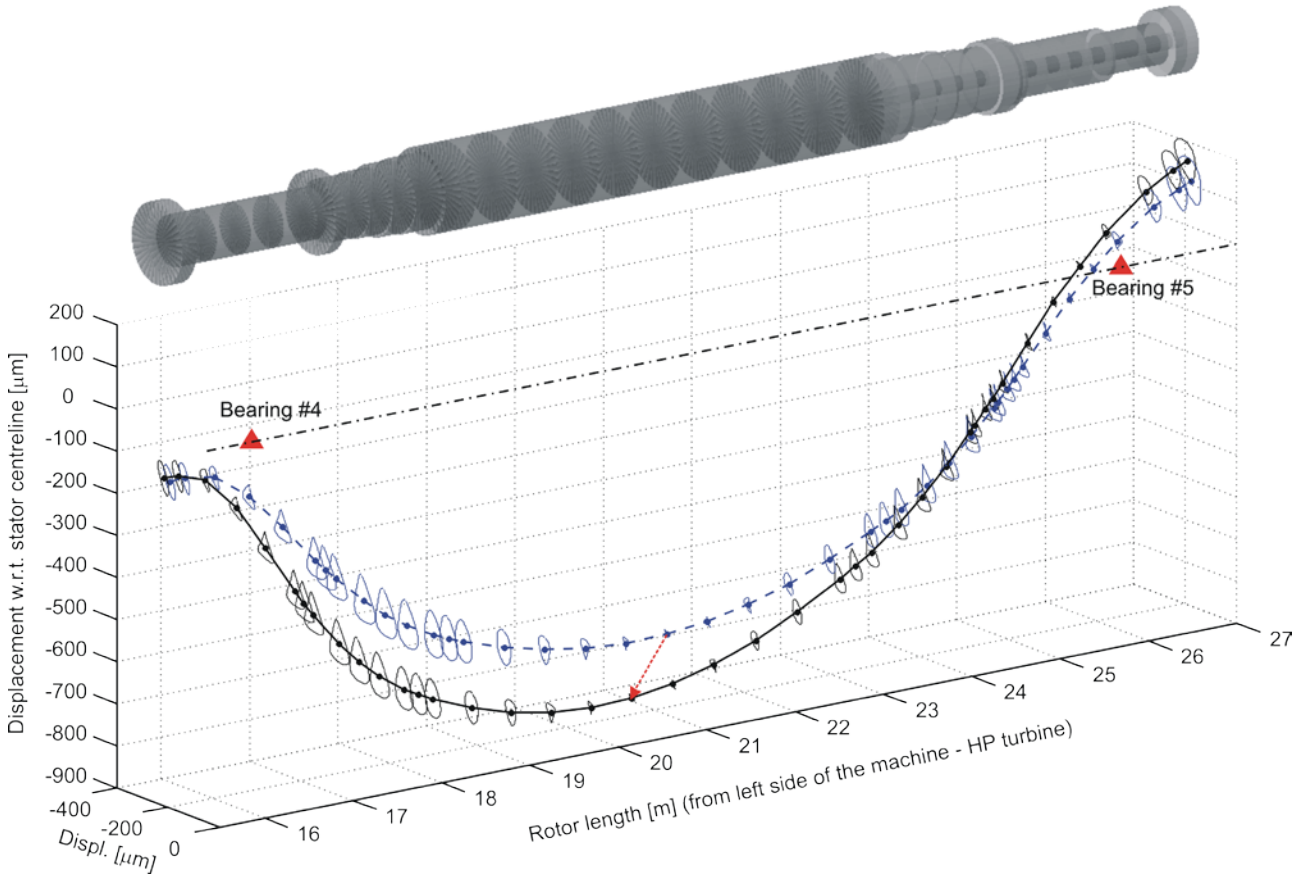

Figure 19: Dynamical behaviour of the generator (dashed line: steady state before excitation, solid line: steady state after excitation).

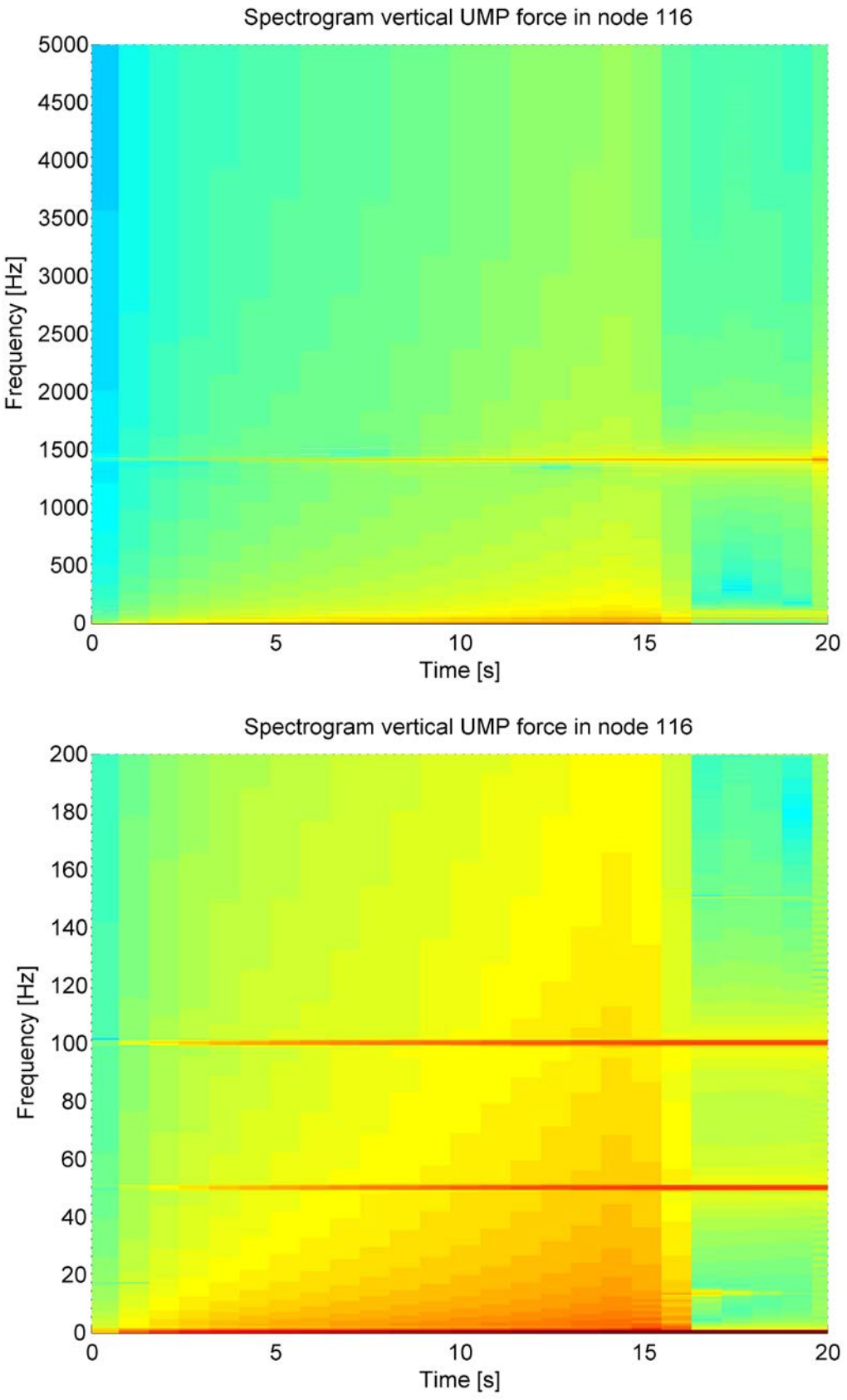

Figure 20: Spectrogram of UMP vertical force in node 116 (mid-span of the generator).

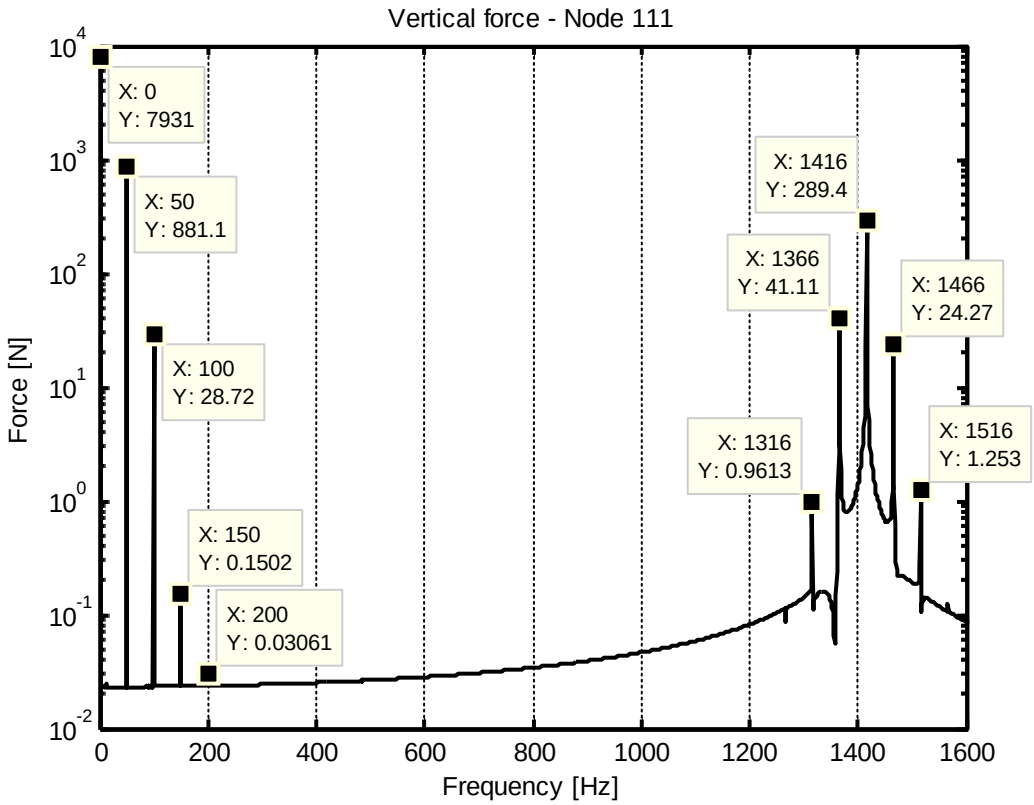

Figure 21: UMP vertical force spectrum in node 111.

Table 1: Comparison between experimental data and simulation results, node 100 – Bearing #4 (Note that experimental orbits are always centred in the origin of reference system S'' (see figure 2) due to the internal conventions of the condition monitoring system, while the simulated ones are referred to S').

Simulated

	Before excitation [μm]	After excitation [μm]	Centreline displacement [μm]
Average, Horizontal	−145.37	−181.34	35.97
1X, Horizontal	18.28@51.34°	17.55@47.29°	
2X, Horizontal	3.78@−142.57°	3.87@−146.01°	
Average, Vertical	−117.6	−131.63	14.03
1X, Vertical	25.27@−80.74°	25.11@−85.01°	
2X, Vertical	2.62@−22.16°	2.67@−25.00°	

Experimental

	Before excitation [μm]	After excitation [μm]	Centreline displacement [μm]
Centreline, Horizontal	-46.8	-77.8	31
1X, Horizontal	18.62@51.60°	19.36@43.49°	
2X, Horizontal	3.90@−141.50°	3.35@−144.3°	
Centreline, Vertical	347	336	11
1X, Vertical	23.62@−80.61°	25.62@−89.29°	
2X, Vertical	2.87@−21.45°	2.01@−20.21°	

Table 2: Comparison between experimental data and simulation results, node 133 – Bearing #5 (Note that experimental orbits are always centred in the origin of reference system S'' (see figure 2) due to the internal conventions of the condition monitoring system, while the simulated ones are referred to S').

Simulated

	Before excitation [μm]	After excitation [μm]	Centreline displacement [μm]
Average, Horizontal	−200.18	−261.44	61.26
1X, Horizontal	4.50@−134.59°	4.03@−140.26°	
2X, Horizontal	8.61@−161.11°	8.82@−164.56°	
Average, Vertical	−120.81	−142.49	21.68
1X, Vertical	8.89@135.81°	7.89@130.04°	
2X, Vertical	4.52@−27.45°	4.61@−30.22°	

Experimental

	Before excitation [μm]	After excitation [μm]	Centreline displacement [μm]
Centreline, Horizontal	-28.38	-84.04	55.7
1X, Horizontal	4.14@−138.9°	5.5@−128.5°	
2X, Horizontal	8.74@−161.2°	9.01@−152.6°	
Centreline, Vertical	197.8	176.9	20.9
1X, Vertical	8.41@134.5°	8.52@136.2°	
2X, Vertical	4.59@−26.75°	4.96@−33.8°	